Objects Interacting with Solidification Fronts: Thermal and Solute Effects

Sidhanth Tyagi[1,2], Hélène Huynh[1], Cécile Monteux[2,3], and Sylvain Deville[1,4,5]

[1]*LSFC, UMR 3080 CNRS/Saint-Gobain CREE, Saint-Gobain Research Provence, 84300 Cavaillon, France*

[2]*Sciences et Ingénierie de la Matiére Molle, ESPCI Paris, PSL Research University, CNRS, Sorbonne Universités, UPMC Univ Paris 06, 75005 Paris, France.*

[3]*Global Station for Soft Matter, Global Institution for Collaborative Research and Education, Hokkaido University, Sapporo, Japan.*

[4]*now with: Université de Lyon, Université Claude Bernard Lyon1, CNRS, Institut Lumière Matière, 69622 Villeurbanne, France.*

[5]*Corresponding author. Email: sylvain.deville@univ-lyon1.fr.*

March 30, 2020

In many materials processing routes, objects such as bubbles or particles interact with a moving solidification front. The output of this confrontation, from instantaneous encapsulation to complete rejection of objects, regulates the solidified microstructure and the spatial distribution of the objects, and thus the final properties of the materials. Here we investigate by *in situ* cryo-confocal microscopy how thermal conductivity and solute compete to control the interfacial curvature of the solidification front. We first validate the prediction of physical models in absence of solute, and then demonstrate the dominating effect of solute. In the case of cellular front morphol-

1

ogy, we show that thermal effects depending on the particle conductivity induce a distortion of ice crystals thereby modifying the final microstructure of the solid. Overall our results show that to successfully predict and control solidification microstructure in the presence of objects, physical models that take into account both thermal and long-range solute effects are now required.

The interaction of solidification fronts with objects (droplets, bubbles, solid particles or cells) is a common phenomenon encountered in a plethora of situations, ranging from industrial to natural occurrences, such as the formation of sea ice, growth of single crystals, metallurgy, cryobiology, or food science. The objects (soft or hard) exhibit different types of behavior while interacting with a solidification front, from total rejection to complete or partial engulfment [2]. The dynamics of this interaction influences the solidified microstructure and the mechanical and functional properties of the materials. From homogeneous particle distribution in particle-reinforced metal matrix composites to complete rejection of inclusions or porosity management in castings and growth of single crystals, distinct outcomes may be desired depending on the application. The potential to actively govern the solidification microstructure is thus crucial. The initial studies performed on encapsulation and/or rejection of particles by a freezing front, moving at a velocity V_{sl}, considered either the interplay of van der Waals and lubrication forces [5] or the change in chemical potential [25]. Most of these physical models established a criterion of critical velocity (V_c), for a given size of an insoluble object or *vice-versa* (critical radius), to predict whether the object will be encapsulated ($V_{sl} > V_c$) or rejected ($V_{sl} < V_c$) [2].

Subsequently, the studies performed showed that the curvature of the solidification front plays a major role in solidification dynamics, as it influences the magnitude of both viscous and van der Waals forces in the gap between the particle and the front. Theoretically, the critical velocity reduces drastically for

2

concave interfaces as opposed to ideal planar interfaces [11].

The disjoining pressure, arising in the gap between the growing solid and the particle, causes a deformation of the solidification front. However, it has been predicted that the thermal conductivity deforms the front 10^3 times more than the other parameters [18]. If a particle has a lower thermal conductivity than the melt $(k_p/k_m < 1)$, the solidification front bulges towards the object and repels it. In the opposite case $(k_p/k_m > 1)$, the solidification front bends away from the particle and facilitates its encapsulation [27]. However, few experimental observations exist to ratify these numerical simulations, owing to the associated small time and space scales, as well as high temperatures of solidification, especially for metals [17, 25].

The thermal conductivity ratio criterion is not extensive and has been contrary in certain experimental predictions of repulsion and engulfment of foreign particles [23]. The presence of solute in the melt may also influence the interaction between a particle and a solidification front, as solutes are rejected by the solid and segregate at the solid-melt interface, leading to a colligative depression of the melting temperature.

Here, we demonstrate in a systematic manner the influence of thermal conductivity on the front curvature using *in situ* cryo-confocal microscopy. We depict that solute segregation at the front overrides thermal conductivity effects and hence, not only controls the interfacial curvature but also the dynamics of particle capture. Furthermore, in the case of cellular front morphology, insulating particles, engulfed in the solid, induce a distortion of the surrounding ice crystals due to persisting local temperature gradients, thereby modifying the final microstructure of the solid.

Thermal conductivity controls the interfacial curvature

We perform solidification experiments with dilute aqueous dispersion of droplets, bubbles, and particles, of similar diameter $\approx 50\,\mu m$, but varying thermal conductivity. We regulate the front velocity (V_{sl}) by translating a Hele-Shaw cell,
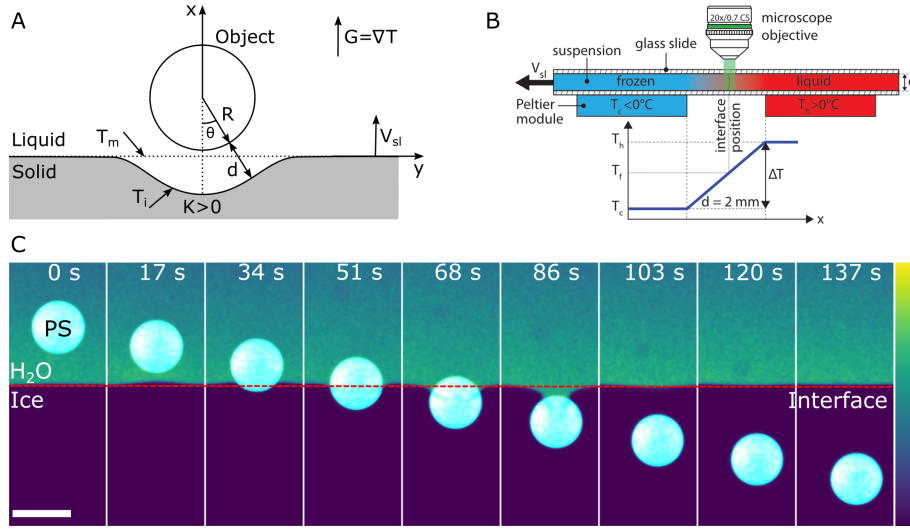
Figure 1: **Objects interacting with a moving solidification font: principles and *in situ* confocal microscope imaging.** (A) Model, sketch. (B) Experimental setup for *in situ* solidification experiments. A thin Hele-Shaw cell containing the suspension, emulsion or foam is pulled at a constant velocity (V_{sl}) through a constant temperature gradient (G) established by Peltier elements. In steady state, the solidification front is thus at a constant position under the microscope objective. (C) Typical time lapse for a freezing particle-in-water suspension with a Polystyrene (PS) particle. The solidification front develops a bump ($t \approx 17s$) in the vicinity of the low thermal conductivity solid ($k_p/k_m < 1$). PS is in cyan, water in colormap viridis (fluorescence bar) while ice is in black. Scale bar $= 50 \, \mu m$. $^{\copyright}$ (2020) S. Tyagi *et al.* (10.6084/m9.figshare.12046560) CC BY 4.0 license https://creativecommons.org/licenses/by/4.0/.

under a confocal laser scanning microscope, along a temperature gradient (G) imposed by two Peltier modules, as shown in Fig. 1. The independent selection of the two parameters (V_{sl} & G) in our setup enables a uniform cooling rate and an improved control over the front morphology.

We observe a pronounced convex curvature (Fig. 2A) when the objects are thermally insulating compared to water ($k_p/k_m < 1$) and thus, the front tends to diverge towards them as they act as thermal shields causing the temperature in the gap behind them to be successively lowered. We used zirconia and stainless steel conducting particles and obtain a cusping of the front (Fig. 2A). The relatively higher thermal conductivity of the spheres ($k_p/k_m > 1$) enables a preferential heat flux from the melt to the front resulting in a concave depression.

4

⁹⁵ Thus, the differing thermal conductivities result in a distortion of the isotherms
⁹⁶ away from the horizontal. The magnitude of the depression (convex or concave)
⁹⁷ depends on the thermal conductivity ratio of the particle to the melt (k_p/k_m)
⁹⁸ (Fig. 2B).

⁹⁹ These observations are in agreement with the numerical model from Park
¹⁰⁰ *et al.* [18]. This model is based on the computation of the particle velocity
¹⁰¹ when it is close to the front $(d << R)$ and takes into account the balance of
¹⁰² hydrodynamic and intermolecular forces, solidification front surface energy, con-
¹⁰³ trast of the particle and melt thermal conductivities, and the flow caused by
¹⁰⁴ the density change upon solidification. It encompasses an asymptotic analysis
¹⁰⁵ in the lubrication approximation and theoretically predicts the curvature of the
¹⁰⁶ front as a function of γ and (k_p/k_m), shown in Fig. 2C, where γ is a dimen-
¹⁰⁷ sionless surface energy parameter, $\gamma = (T_m \sigma_{sl})/(L_v G R^2)$, where T_m is the bulk
¹⁰⁸ melting temperature at constant pressure, G is the applied temperature gradi-
¹⁰⁹ ent, σ_{sl} is the interfacial tension between the solid and the melt, of the order
¹¹⁰ $3 \times 10^{-2} \, Nm^{-1}$, and R is the radius of the spherical object. Our solidification
¹¹¹ experiments correspond to $\gamma \approx 3.5 \times 10^{-3}$. We can see from Fig. 2C that when
¹¹² $k_p/k_m > 1$, the front is always concave and has a depression away from the
¹¹³ object. While for $k_p/k_m < 1$, three curvatures are feasible corresponding to
¹¹⁴ concave, concave-convex, and convex. The domain of concave-convex geometry
¹¹⁵ is limited to higher γ regions while it reduces to a confined zone when k_p/k_m
¹¹⁶ is close to 1 and $\gamma < 10^{-1}$. We could not investigate this region as it requires
¹¹⁷ either the use of minute objects $(R < 5 \, \mu m)$ or the application of a small tem-
¹¹⁸ perature gradient $(G < 1 \times 10^2 \, Km^{-1})$, other parameters being constant for
¹¹⁹ the particle-in-water system. While using minute objects is inconceivable as
¹²⁰ the interfacial curvature would be below the optical spatial resolution, using a
¹²¹ smaller temperature gradient would render a planar front thermodynamically
¹²² unstable owing to the supercooling [13].

¹²³ Interestingly, there seems to be no conspicuous digression in the dynamics of
¹²⁴ objects with $k_p/k_m < 1$ or $k_p/k_m > 1$, which depict similar behaviour as can be

₁₂₅ seen in the time-lapse figure (Fig. 1C). We do not observe repulsion of neither

₁₂₆ the soft objects (oil droplet and air bubble) nor the insulating rigid particles in

₁₂₇ the system investigated, which rather tend to be encapsulated instantaneously.

₁₂₈ This trend is contrary to the previous studies [2], where a convex front tends

₁₂₉ to increase the critical engulfment velocity (V_c) and facilitates repulsion of the

₁₃₀ object through a reduction of lubrication drag forces in the gap between the

₁₃₁ particle and the front [18].

₁₃₂ All these predictions and results were obtained so far in pure systems. How-

₁₃₃ ever, almost all real melt systems consist of solutes in some form or the other,

₁₃₄ be it desired (for imparting better mechanical and/or physical properties) or

₁₃₅ undesired (such as impurities, inclusions etc...). It has been shown recently

₁₃₆ that the dynamics of interaction of an object with a solidification front and the

₁₃₇ critical role of solutes have been highly underestimated in the studies so far [7].

₁₃₈ We cannot use the existing models as they consider a dominant role of ther-

₁₃₉ momolecular forces, which are effective only at very short distances ($\sim 10^{-10}$

₁₄₀ m) [2, 18, 21], while solute fields are long range($\sim 10^{-4}$ m) [2, 7]. We therefore

₁₄₁ investigate how solute impacts the interfacial curvature.

Solute effects override thermal conductivity effects

₁₄₃ We carried out freezing experiments with the same set of objects (oil droplets,

₁₄₄ gas bubbles, and particles) in the presence of $1wt.\%$ TWEEN80 (acting as a

₁₄₅ model solute) aqueous phase. This surfactant, needed to stabilize the bubbles

₁₄₆ and drops, is used here as a model solute that decreases colligatively the freezing

₁₄₇ point in all systems. We assume the thermal conductivity ratio of the objects

₁₄₈ to melt remains the same as shown in Fig. 2C. Thermal conductivity is a ma-

₁₄₉ terial property that depends primarily on temperature, and thus we expect no

₁₅₀ significant changes to its value while adding small amounts of solute to water.

₁₅₁ We observed only convex interfacial curvature in the absence of solute with

₁₅₂ $k_p/k_m < 1$, however, in the presence of solute, solely concave curvatures are

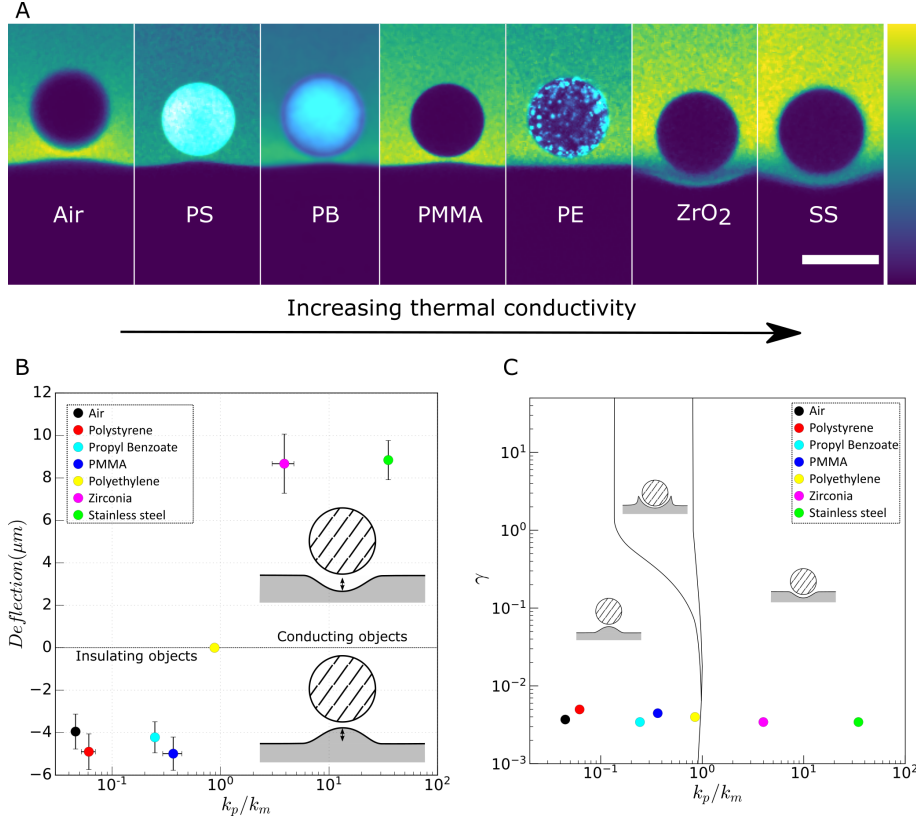₁₅₃ observed (Fig. 3A). In the presence of conducting objects with $k_p/k_m > 1$, the

6

Figure 2: **Thermal conductivity effects on interfacial curvature in absence of solute.** (A) Insulating air-in-water bubble, polystyrene (PS) particle, propyl benzoate (PB) droplet, and Poly(methyl methacrylate) (PMMA) particle promote a convex curvature of the solidification front. Polyethylene (PE) particle does not affect the curvature. Conducting zirconia (ZrO_2) and stainless steel (SS) particles result in a concave depression. We added a very small amount ($0.01wt.\%$) of TWEEN80 to stabilise the foam and the emulsion, while no solute was present for the particle suspensions. PS, PB, and PE are in cyan, water in colormap viridis (fluorescence bar) while ice, air, PMMA, zirconia, and stainless steel are in black. Scale bar $= 50\,\mu m$. (B) Plot of front deflection versus ($\boldsymbol{k_p/k_m}$) for solidification of spherical objects in absence or at low concentration of solute. (C) Three distinct curvatures of the solidification front in the thermal conductivity ratio ($\boldsymbol{k_p/k_m}$) versus $\boldsymbol{\gamma}$ plane for a spherical particle, adapted from Park *et al.* [18].

front exhibits a much more pronounced concave depression as compared to the geometry observed in the absence of solutes (Fig. 4). Thus, the solute tends to play a dominant role and renders the solidification front concave regardless of the thermal conductivity ratio.
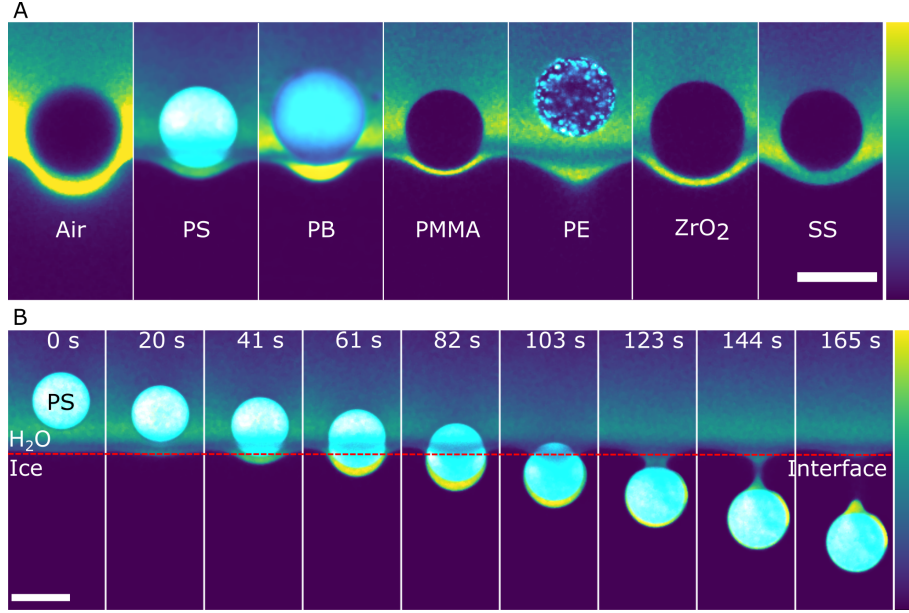
Figure 3: **Impact of solute on the front curvature.** (A) Concave depression of the solidification front with air bubble, polystyrene (PS), propyl benzoate (PB), poly(methyl methacrylate) (PMMA), polyethylene (PE), zirconia (ZrO_2), and stainless steel (SS) particles. PS, PB, and PE are in cyan, water in colormap viridis (fluorescence bar) while ice, air, PMMA, zirconia, and stainless steel are in black. Scale bar = $50\,\mu m$. (B) Typical time-lapse for a freezing particle-in-water suspension, with a PS particle, in the presence of solute: $1wt.\%$ TWEEN 80. The solidification front bends away from the solid ($t \approx 41s$) and eventually heals leaving a premelted film around the encapsulated particle. PS is in cyan, water in colormap viridis (fluorescence bar) while ice is in black. Scale bar = $50\,\mu m$. © (2020) S. Tyagi *et al.* (10.6084/m9.figshare.12046560) CC BY 4.0 license https://creativecommons.org/licenses/by/4.0/.

As an insoluble object approaches a solidification front, it obstructs the diffusion field, and leads to a build-up of solutes (rejected by ice) at the front. Since growth from solutions depends on the concentration gradient of solutes at the front, the liquidus temperature of the melt differs from the melting temperature of the bulk composition. The change in liquid composition alters its transformation temperature, referred to as constitutional supercooling [24]. Therefore, the solute-rich region colligatively depresses the freezing point of the aqueous phase. This distortion of the isotherm away from the horizontal manifests itself as the concave depression of the solidification front. The resulting thin film, visible in the high fluorescence crescent (Fig. 3) between the object and the
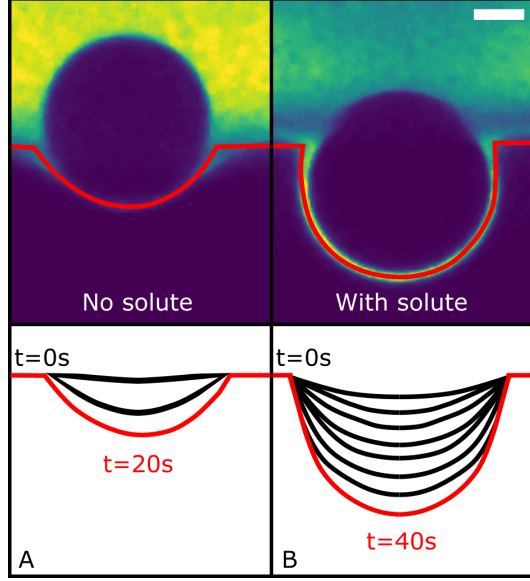
8

Figure 4: **Maximum interfacial curvature depression with time observed before encapsulation, in absence (A) and presence (B) of solute; $1wt.\%$ TWEEN80, for a conducting zirconia particle ($k_p/k_m >$ 1).** Scale bar $= 20\,\mu m$ © (2020) S. Tyagi *et al.* (10.6084/m9.figshare.12046560) CC BY 4.0 license https://creativecommons.org/licenses/by/4.0/.

growing ice, is driven by the tendency to reduce the interfacial free energy and known as a premelted film [4, 20, 26]. The films are thermodynamically stable below their bulk melting temperature and are extremely sensitive to the presence of solutes (known as solute premelting). The solute premelted films are quite evident in these experiments (Fig. 3B), however, we do not observe any interfacial premelting in the absence or at low concentrations of solute (Fig. 1C). The concave curvature of the front facilitates lateral solute diffusion causing the front to accelerate, while engulfing the object with a solute-rich premelted film around it.

These results depart from the behaviour predicted in most physical models, where thermal fields are expected to affect the curvature of the solidification front [2]. We believe the long-range solute field interactions (with a length scale of $\sim D/V$) dominate over the short-range thermomolecular forces. This enforces the importance of purely diffusive (solute) effects during solidification as they

not only alter the interfacial curvature but also the nature and equilibrium of forces on the particle. Solutes impact the premelted film thickness [26], viscosity, undercooling [21], and can induce phoresis of suspended objects [1, 7] during freezing. Therefore, the prediction of the object behaviour when it encounters a solidification front is not so trivial. We suggest that the criterion of thermal conductivity ratio (k_p/k_m), for concluding whether an object will undergo engulfment or rejection, needs to be modified to account for long-range solute field interactions. However, modelling of the solute effects is beyond the scope of this study.

Solute and thermal conductivity effects in cellular growth

We have discussed so far the interfacial geometry for an ideal planar front morphology preceding particle encapsulation. We will now focus on the breakdown of the planar front and the subsequent impact of thermal conductivity mismatch, when a particle is engulfed. Most realistic systems present a scenario where a planar shape is thermodynamically not stable. This can be attributed to a high freezing velocity, constitutional supercooling, and the complete rejection of solutes from the solid phase, which produces a severe concentration gradient at the front [16, 24]. The resulting perturbations destabilise a *steady-state* planar front into regularly spaced cells through the propagation of Mullins-Sekerka instability [15]. Although these instabilities have been investigated for a long time, we are not aware of any available quantitative models describing the capture of isolated single particles by a non-planar (cellular or dendritic) front morphology.

At high solidification velocity ($V_{sl} = 10 \times 10^{-6}\,ms^{-1}$) with $1wt.\%$ TWEEN80 in the aqueous phase, we obtain a cellular front morphology with solute-rich grain boundaries (Fig. 5). For bubbles (Fig. 5A), the front tends to be moderately convex ($t \approx 3s$) with a deflection away from the horizontal, owing to the extremely low thermal conductivity of air, while it transforms into a concave depression in the proximity of the bubble ($t > 3s$). For the oil-in-water emulsion (Fig. 5B), the solidification front stays at the same ordinate before the
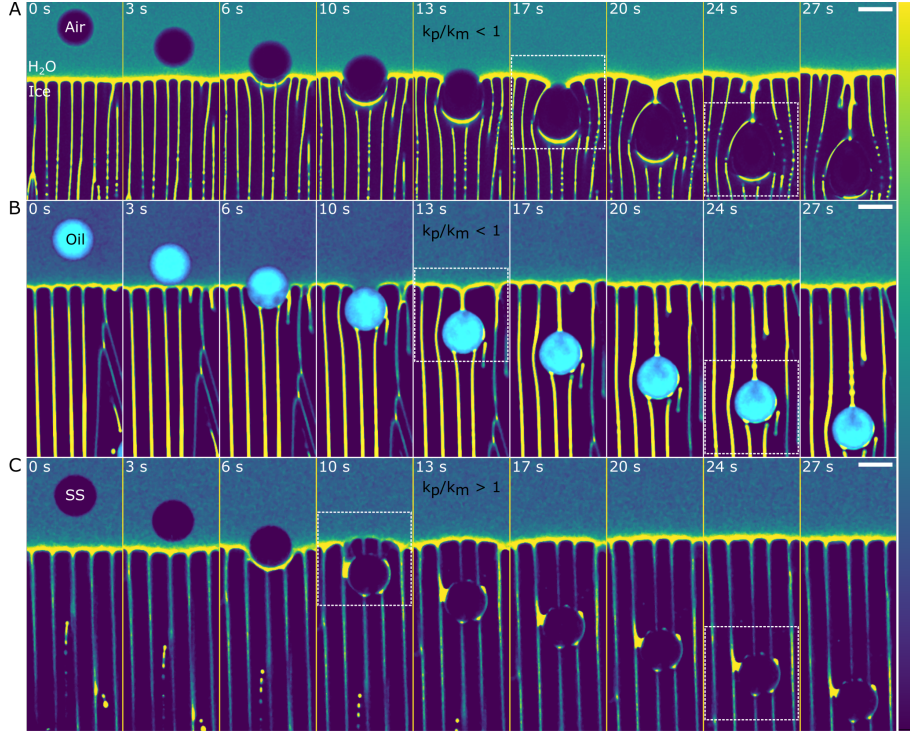
10

Figure 5: **Deformation of the grain boundaries and blunting of the ice tip radius at the solidification front during encapsulation.** (A, B, and C) Time-lapse of oil-in-water emulsion (A) with $G = 10\ Kmm^{-1}$, air-in-water foam (B) with $G = 15\ Kmm^{-1}$, and stainless steel sphere (SS) (C) with $G = 10\ Kmm^{-1}$, at $V_{sl} = 10 \times 10^{-6}\ ms^{-1}$. Oil is in cyan, water in colormap viridis (fluorescence bar) and ice, air, and SS are in black. Scale bar $= 50\,\mu m$.

211 droplet impingement ($t < 3s$), contrary to the depression in planar morphology

212 (Fig. 3A). The stainless steel particles (Fig. 5C), being highly conductive, in-

213 duce a concave cusping of the front ($t \approx 3s$), which is further enhanced by the

214 constitutional supercooling ($t \approx 6s$).

215   The solutes are partially segregated into the grain boundaries and hence, the

216 effective concentration gradient at the ice-water front is considerably reduced

217 compared to the previous planar front situations. Cellular fronts redistributes

218 the rejected solutes parallel to the temperature gradient. This diminishes the

219 extent of constitutional supercooling, thereby averting an extensive cusping of

220 the front and preventing a dominant role of solutes before encapsulation. Thus,

the effective distance, between the object and the ice, at which solutes modify the interfacial geometry of a cellular front is considerably smaller.

After encapsulation, the insulating particles ($k_p/k_m < 1$)(Fig. 5A, 5B) deform the grain boundaries in their vicinity ($t > 10s$) and alter the ice tip radius. We believe the thinning of the grains around these particles is essentially related to the local temperature gradients originating from the difference in thermal conductivity ratio between the particle and the encircling crystal. The objects remain at relatively higher temperatures for sufficient amount of time to modify the solidified microstructure. Indeed, the grain boundaries do not undergo geometrical modifications (Fig. 5C) with stainless steel sphere, as it is highly conductive ($k_p/k_m > 1$), and therefore, homogenises its temperature with the surrounding ice instantaneously.

The rapid cryo-confocal microscopy enables us to follow *in situ* the evolution of the microstructure. The front eventually heals and recovers its original cellular spacing, which is a function of temperature gradient, solidification velocity, and solute concentration gradient [15, 24]. The freezing of suspensions with a cellular front is an attractive route for processing porous ceramics, metals, and even composites [8]. An improved understanding of the critical parameters is thus desired to regulate the front morphology and the resulting material properties [9]. The size and spacing of grains is an indispensable attribute controlling the mechanical properties of a polycrystalline material (*Hall-Petch relationship*) [12, 19]. Consequently, the heterogeneous microstructure can be detrimental to an otherwise homogeneous finished product. Thus, solutes play a key role in solidification and an in-depth understanding of their redistribution mechanism is required.

Conclusions

Cryo-confocal microscopy [7] exhibits great promise for the *in situ* analysis of solidification mechanisms with foreign objects. We have demonstrated the role of thermal conductivity mismatch on the distortion of solidification fronts in

the absence of solutes. Furthermore, our results show that both insulating and conducting particles get engulfed by the front in contrast to previous theoretical and numerical studies. In the presence of solute, the long-range solute field interactions play a critical role on the front curvature and the evolution of the solidification microstructure. With cellular front morphology, local temperature gradients around the engulfed particles distort grain growth and further work is required to correlate these observations to analogous real life systems. We hope our extensive research with ceramics, metals, and polymers serves for the formulation of a robust physical model with the incorporation of solute effects.

Experimental section

Materials

Propyl Benzoate, TWEEN80, Difluoro2-[1-(3,5-dimethyl-2H-pyrrol-2-ylidene-N)ethyl]-3,5-dimethyl-1H-pyrrolato-Nboron (BODIPY), and Sulforhodamine B (SRhB) were obtained from Sigma-Aldrich. Zirconia (ZrO_2) spheres (Zirmil Y from Saint-Gobain ZirPro, $50-63\,\mu m$) were provided by Saint-Gobain Research Provence. We purchased fluorescent green Polyethylene ($1\,g\,cm^{-3}$, $45-53\,\mu m$) and Stainless Steel ($7\,g\,cm^{-3}$, $48-57\,\mu m$) microspheres from Cospheric LLC. We ordered monodisperse green-fluorescent Polystyrene ($48.1\,\mu m$) and Poly(methyl methacrylate) (PMMA) ($50.3\,\mu m$) from Micro Particles GmbH. Deionized water, filtered with 0.45 μm Nylon membrane filters (VWR International), was used for the aqueous phase. The thermal and geometrical parameters which were important for our study are given in table 1 below. The material properties have values based on their typical conditions at 25°C and 1 atm.

Sample Preparation

The oil-in-water emulsions were prepared by using a microfluidic setup (microfluidic starter kit, Micronit Microfluidics, Netherlands) with pressure controlled flow pumps (Fluigent LineUP Flow EZ) and uncoated focused flow

13

Particle	R (m)	k_p $(Wm^{-1}K^{-1})$	k_p/k_m
Air	27×10^{-6}	0.026	0.046
Polystyrene (PS)	24×10^{-6}	0.030 - 0.040	0.052 - 0.070
Propyl Benzoate (PB)	28×10^{-6}	0.141	0.248
PMMA	25×10^{-6}	0.167 - 0.250	0.293 - 0.439
Polyethylene (PE)	26×10^{-6}	0.500	0.879
Zirconia (ZrO$_2$)	28×10^{-6}	1.7 - 2.7	2.988 - 4.745
Stainless Steel (SS)	28×10^{-6}	20.0	35.149

Table 1: Radius (R), thermal conductivity of the materials (k_p) and their ratio with the aqueous phase (k_p/k_m), where $k_m = 0.569 \, Wm^{-1}K^{-1}$.

droplet generator chips (FF_DROP), with a nozzle diameter of $50 \, \mu m$. The flow rate of oil and aqueous phases were controlled using Fluigent Flow Unit S ($0 - 7 \, \mu L/min$). The oil phase consisted of propyl benzoate with $10^{-4} \, M$ BODIPY, and the aqueous phase was a $10^{-5} \, M$ SRhB solution. The air-in-water foams were prepared by using the double syringe technique [10], with a luer adapter as connective, and a liquid fraction of 50 %. For the foams, we bubbled air through liquid perfluorohexane (C_6F_{14} 98+%, Alfa Aesar) to obtain a gas composed of air and perfluorohexane vapour. Thus, we could delay coarsening [3] and ensure the bubbles remained stable during the experimental time-scales, typically varying from 4 to 6 hours at $V_{sl} = 10^{-6} \, ms^{-1}$. TWEEN80 was used as a non-ionic surfactant and solute to avoid long-range electrostatic interactions. We used the same surfactant for stabilising both the oil-in-water emulsions and the air-in-water foams. The particle suspensions were thoroughly sonicated ($30 - 40 \, min$) to ensure a homogeneous dispersion. The experiments in the presence of solute were carried out by adding $1wt.\%$ TWEEN80 to the aqueous phase. We used the same solute and concentration for all systems to ensure comparable results. The solutions were frozen in a rectangular Hele-Shaw cell (h = 100 μm and V = 100 μl), fabricated using two glass slides (Menzel, $24 \times 60 \, mm$, thickness $0.13 - 0.16 \, mm$), and sealed with nail-polish at one end to avoid evaporation.

Freezing Stage

We performed directional freezing experiments, translating the sample along a constant linear temperature gradient of $10\,Kmm^{-1}$, using the cryo-confocal stage described previously [6]. We carried out all the experiments at $V_{sl} = 10^{-6}\,ms^{-1}$, unless stated otherwise. The solidification front tends to appear immobile in the frame of observation, however, in the sample frame, it is the ice solidifying (along $\vec{x}$) at the velocity imposed by the pulling rate of the motor (Micos Pollux Drive VT-80 translation stage PI, USA). We modified the stage by substituting the aluminium plate with a copper serpentine sheet and discarding the silicon carbide honeycomb interface. This led to an improved stability and a more robust cooling setup. The temperature gradient was imposed with two Peltier modules and controlled using TEC-1122 Dual Thermo Electric Cooling Temperature Controller from Meerstetter Engineering, Switzerland. We can thus decouple and control independently the solidification velocity (V_{sl}) and the temperature gradient (G).

Imaging & Analysis

The images were acquired through a Leica TCS SP8 confocal laser scanning microscope (Leica Microsystemes SAS, Germany), equipped with $488\,nm$ (blue) and $552\,nm$ (green) lasers. We utilised the microscope at a scanning speed of $600\,Hertz$, with $1024 \times 1024\,pixels$ for imaging $775 \times 775\,\mu m$, resulting in $1.7\,seconds$ per frame. The high spatial resolution, coupled with rapid screening, enabled us to observe the dynamics of objects interacting with solidification fronts *in situ*. We used two photodetectors (PMT) to simultaneously image three phases :

1. BODIPY (λ_{ex} $493\,nm$; λ_{em} $504\,nm$), the dye incorporated into the oil droplets. The same emission spectrum was utilised to image the fluorescent colloids.

2. SRhB (λ_{ex} $565\,nm$; λ_{em} $586\,nm$), dissolved in water, to image the aqueous

15

phase and the grain boundaries in ice.

3. Ice, does not fluoresce, as it has very low solubility for solutes [14] and hence, appears black.

The emission spectra of the excited fluorophores was captured using a non-immersive objective (Leica HCX PL APO CS 20×). The working distance of $590\,\mu m$ and an insulating foam cover facilitates the minimization of thermal perturbations on the freezing substrate. We used Fiji [22] and Python for image processing and data analysis.

Typical solidification parameters

Parameters	Particle in water
G (Km^{-1})	$1.0\ \times 10^4$
T_m (K)	273.15
L_v (Jm^{-3})	3.03×10^8
σ_{sl} (Jm^{-2})	$3.0\ \times 10^{-2}$
V_{sl} (ms^{-1})	$1.0\ \times 10^{-6}$
λ (m)	2.83×10^{-10}

Table 2: Typical solidification parameters for an object in front of an ice-water solidification front. L_v, σ_{sl}, and λ adapted from Park *et al.* [18]

Acknowledgements

Author contributions

S.D. and C.M. designed and supervised the project, S.D, C.M. and S.T. designed the experiments, S.T. and H.H. carried out the confocal microscopy, S.T. wrote the code to analyze the data, S.T., C.M. and S.D. analyzed the data. All

authors discussed the results and implications. S.T., C.M. and S.D. wrote the
manuscript.

Conflict of interest

The authors declare no conflict of interest.

References

[1] John L Anderson. Colloid transport by interfacial forces. *Annual review of fluid mechanics*, 21(1):61–99, 1989.

[2] R. Asthana and S. N. Tewari. The engulfment of foreign particles by a freezing interface. *Journal of Materials Science*, 28(20):5414–5425, 1993.

[3] Zenaida Briceño-Ahumada and Dominique Langevin. On the influence of surfactant on the coarsening of aqueous foams. *Advances in colloid and interface science*, 244:124–131, 2017.

[4] J. W. Cahn, J. G. Dash, and Haiying Fu. Theory of ice premelting in monosized powders. *Journal of Crystal Growth*, 123(1-2):101–108, 1992.

[5] AA Chernov, DE Temkin, and AM Mel'Nikova. Theory of the capture of solid inclusions during the growth of crystals from the melt. *Sov. Phys. Crystallogr*, 21(4):369–373, 1976.

[6] Dmytro Dedovets, Cécile Monteux, and Sylvain Deville. A temperature-controlled stage for laser scanning confocal microscopy and case studies in materials science. *Ultramicroscopy*, 195(August):1–11, 2018.

[7] Dmytro Dedovets, Cécile Monteux, and Sylvain Deville. Five-dimensional imaging of freezing emulsions with solute effects. *Science*, 360(6386):303–306, 2018.

[8] Sylvain Deville. Ice-Templated Materials: Polymers, Ceramics, Metals and Their Composites. In *Freez. Colloids Obs. Princ. Control. Use*, chapter 4, pages 253–350. Springer International Publishing, Cham, 2017.

[9] Sylvain Deville, Eric Maire, Guillaume Bernard-Granger, Audrey Lasalle, Agnès Bogner, Catherine Gauthier, Jérôme Leloup, and Christian Guizard. Metastable and unstable cellular solidification of colloidal suspensions. *Nature materials*, 8(12):966, 2009.

[10] T Gaillard, M Roché, C Honorez, M Jumeau, A Balan, C Jedrzejczyk, and W Drenckhan. Controlled foam generation using cyclic diphasic flows through a constriction. *International Journal of Multiphase Flow*, 96:173–187, 2017.

[11] Layachi Hadji. The drag force on a particle approaching a solidifying interface. *Metallurgical and Materials Transactions A*, 37(12):3677–3683, 2006.

[12] EO Hall. The deformation and ageing of mild steel: *iii* discussion of results. *Proceedings of the Physical Society. Section B*, 64(9):747, 1951.

[13] C Körber. Phenomena at the advancing ice-liquid interface: solutes, particles and biological cells. *Quarterly reviews of biophysics*, 21:229–298, 1988.

[14] Moreno Marcellini, Cecile Noirjean, Dmytro Dedovets, Juliette Maria, and Sylvain Deville. Time-Lapse, in Situ Imaging of Ice Crystal Growth Using Confocal Microscopy. *ACS Omega*, 1(5):1019–1026, 2016.

[15] W. W. Mullins and R. F. Sekerka. Stability of a planar interface during solidification of a dilute binary alloy. *Journal of Applied Physics*, 35(2):444–451, 1964.

[16] M. G. O'Callaghan, E. G. Cravalho, and C. E. Huggins. Instability of the planar freeze front during solidification of an aqueous binary solution. *Journal of Heat Transfer*, 102(4):673–677, 1980.

[17] S. N. Omenyi and A. W. Neumann. Thermodynamic aspects of particle engulfment by solidifying melts. *Journal of Applied Physics*, 47(9):3956–3962, 1976.

[18] Min S. Park, Alexander A. Golovin, and Stephen H. Davis. The encapsulation of particles and bubbles by an advancing solidification front. *Journal of Fluid Mechanics*, 560:415, 2006.

[19] NJ Petch. J iron steel inst. *London*, 174(1):25–8, 1953.

[20] A. W. Rempel, J. S. Wettlaufer, and M. G. Worster. Interfacial Premelting and the Thermomolecular Force: Thermodynamic Buoyancy. *Physical Review Letters*, 87(8):088501, 2001.

[21] A. W. Rempel and M. G. Worster. Particle trapping at an advancing solidification front with interfacial-curvature effects. *Journal of Crystal Growth*, 223(3):420–432, 2001.

[22] Johannes Schindelin, Ignacio Arganda-Carreras, Erwin Frise, Verena Kaynig, Mark Longair, Tobias Pietzsch, Stephan Preibisch, Curtis Rueden, Stephan Saalfeld, Benjamin Schmid, et al. Fiji: an open-source platform for biological-image analysis. *Nature methods*, 9(7):676, 2012.

[23] MK Surappa and PK Rohatgi. Heat diffusivity criterion for the entrapment of particles by a moving solid-liquid interface. *Journal of Materials Science*, 16(2):562–564, 1981.

[24] WA Tiller, KA Jackson, JW Rutter, and B Chalmers. The redistribution of solute atoms during the solidification of metals. *Acta metallurgica*, 1(4):428–437, 1953.

[25] D. R. Uhlmann, B. Chalmers, and K. A. Jackson. Interaction between particles and a solid-liquid interface. *Journal of Applied Physics*, 35(10):2986–2993, 1964.

[26] J. Wettlaufer. Impurity Effects in the Premelting of Ice. *Physical Review Letters*, 82(12):2516–2519, 1999.

[27] AM Zubko, VG Lobanov, and V V₋ Nikonova. Reaction of foreign particles with a crystallization front. *Sov. Phys. Crystallogr.*, 18(2):239–241, 1973.